

Grating Perovskite Enhanced Polarization-Sensitive GaAs-Based Photodetector

Chunyan Wu¹, Bin Zeng¹, Kunnan Zhou, Longqiang Shan, Junjie Wang, Li Wang¹, Yizhong Yang¹, Yuxue Zhou, and Linbao Luo¹, *Senior Member, IEEE*

Abstract—In this work, we demonstrate the fabrication of GaAs photodetector with grating perovskite (G-PVK) for a broadband enhanced ultraviolet (UV)-near-infrared (NIR) photodetection. The device shows a peak photoresponse under 530-nm illumination, presenting a responsivity of 0.3 A/W, a specific detectivity of 2.24×10^{10} Jones, and 0.6/0.56 ms for rise/fall time, respectively. Compared to the device without PVK, the dark current was suppressed by two orders of magnitude and the photoresponse was enhanced up to 215%. This should be ascribed to the effective spatial separation of the vertical build-in electric field between GaAs and G-PVK and the enhanced light trapping arising from the diffraction grating. The well-aligned grating also shows a high sensitivity to the polarized light, giving rise to a peak-to-valley ratio I_{\max}/I_{\min} of about 2.14. This suggests the potential application of the device in the polarization-sensitive imaging system.

Index Terms—Diffraction grating, photodetector, polarization imaging.

I. INTRODUCTION

GaAs, a representative of III–V compounds with a direct bandgap of 1.42 eV, has attracted great attention in field of photodetection due to its merits, including high electron mobility, high saturated drift velocity, and wide absorption spectrum from ultraviolet (UV) to near infrared (NIR) [1], [2]. A great variety of photodetectors, including p-n junction diodes [3], phototransistors [4], and photoconductive detectors [5], have been developed. Among them, photoconductive detectors exhibit the prominent production simplicity as well as high gain and high responsivity arising from the trapping

Manuscript received January 27, 2022; revised March 15, 2022; accepted March 17, 2022. Date of publication March 30, 2022; date of current version April 22, 2022. This work was supported in part by the Natural Science Foundation of China under Grant 62074048 and Grant 51902078, and in part by the Fundamental Research Funds for the Central Universities under Grant PA2020GDKC0014. The review of this article was arranged by Editor J. D. Phillips. (Corresponding authors: Yizhong Yang; Linbao Luo.)

Chunyan Wu, Bin Zeng, Kunnan Zhou, Longqiang Shan, Junjie Wang, Li Wang, Yizhong Yang, and Linbao Luo are with the School of Microelectronics, Hefei University of Technology, Hefei 230009, China (e-mail: yangyizhong@hfut.edu.cn; luolb@hfut.edu.cn).

Yuxue Zhou is with the College of Physical Science and Technology, Yangzhou University, Yangzhou 225002, China.

Color versions of one or more figures in this article are available at <https://doi.org/10.1109/TEDE.2022.3160943>.

Digital Object Identifier 10.1109/TEDE.2022.3160943

effect [6]. Inevitably, however, they suffer from a large dark current and a slow response speed, which may impede their application in the field of fast imaging such as real-time trajectory tracking and security monitoring.

Different strategies have been developed to improve the properties of planar photoconductive detectors.

1) *Suppressing the Dark Current*: A vertical heterojunction can effectively manipulate the dark current of a photoconductive detector. For example, by introducing a p-GaN cap, the two-dimensional electron gas at the AlGaN/GaN heterointerface can be effectively depleted and the dark current was suppressed to 29 pA/mm [7]. Meanwhile, due to the spatial separation of electrons and holes, the carrier recombination activity is significantly reduced, leading to a higher gain and responsivity [8].

2) *Accelerating the Separation of Photogenerated Electron–Hole Pairs (EHPs)*: For a metal Schottky contact, the EHPs generated within the depletion region will be rapidly separated by the build-in electric field. Therefore, metal–semiconductor–metal (MSM) photodetectors present a high speed than the planar photoconductive detectors [9]. Furthermore, to overcome the uniform electric field within the planar GaAs MSM detectors, Marago *et al.* [10] adopted recessed electrodes. A shortened distance for photocarriers to reach the electrodes reduced the long falling tail in the temporal response, giving a response time of 0.9 ps without any expense of the responsivity.

3) *Enhancing Light Absorption*: Constructing optical structure to enhance light absorption provides an effective way to improve the utilization rate of incident light in optoelectronic devices [11]–[13]. Wang *et al.* [14] proved that the average reflectivity of pure GaAs wafer could be reduced from 35% to 2.3% by etching submicrometer GaAs cone arrays. Optical structured perovskite, including nanogratings [15], resonators [16], and photonic crystals [17], have also been widely used due to their ease processibility. For example, inspired by the microstructure on butterfly wings, Li *et al.* [18] fabricated a 1-D nanograting bonded porous 2-D photonic crystal perovskite photodetector (G-PC-PD). The coupling effect of grating diffraction and the PC stopband rendered a responsivity up to 12.6 A/W, which was 6–7 times that of its planar counterpart. Recently, Ruddlesden–Popper (RP)

layered perovskites with alternately stacked inorganic perovskites (wells) and bulky organic spacers (barriers) stand out. The hydrophobic bulky organic cations provide an outstanding moisture stability, while the inorganic perovskites function well as the in-plane charge conductive channels [19], [20].

Here, we propose the GaAs photodetector with grating $\text{PEA}_2\text{MA}_3\text{Pb}_4\text{I}_{13}$ perovskite (G-PVK) for broadband photodetection, which exhibits significantly enhanced photoresponse during the broadband wavelength region (365–970 nm) compared to GaAs photodetectors without G-PVK. The device presents a responsivity of 0.3 A/W, a specific detectivity of 2.24×10^{10} Jones, and a fast response speed (0.6 and 0.56 ms for rise and fall time, respectively). What is more, it shows a high sensitivity to the polarized light, giving a peak-to-valley ratio I_{\max}/I_{\min} of about 2.14. This suggests the potential application of the device in the polarization-sensitive imaging system.

II. EXPERIMENTS

A. Device Fabrication

For the fabrication of the polarization-sensitive GaAs-based photodetector, the pre-cleaned n-type GaAs substrate (resistivity: $8 \times 10^{-4} - 9 \times 10^{-3} \Omega\cdot\text{cm}$) was treated by oxygen plasma for 10 min to obtain a hydrophilic surface and G-PVK was fabricated according to the previously reported nanochannel-confined growth strategy [21]. In a typical process for preparing the well-aligned G-PVK, 0.25-mmol PEA₂MA₃Pb₄I₁₃ precursor solution was dropped onto the hydrophilic GaAs substrate to form a thin precursor film, followed by imprinting of a piece of PDMS template, which was obtained by utilizing a commercially available DVD-R as the master template. The substrate with the PDMS template was then placed in a vacuum drying oven and kept at 55 °C for 9 h with the chamber pressure set to be 0.03 MPa. The PDMS template was peeled off after the solvent was completely evaporated, leaving the well-aligned G-PVK on the substrate. The substrate with G-PVK was annealed at 90 °C for 15 min. to obtain a better crystallinity. A pair of Au electrodes (50 nm) was deposited onto the substrate by electron beam evaporation through a lab-built shadow mask, showing the channel length 1500 μm, channel width 100 μm, and the direction parallel to G-PVK. A control GaAs device without G-PVK was also fabricated for comparison.

B. Device Characterization

Photoelectronic characterization of the device was carried out on a semiconductor characterization system (Keithley 4200-SCS). The laser diodes with different wavelengths (Thorlabs, 365–970 nm) were used as light sources and the power intensities were carefully calibrated using a power

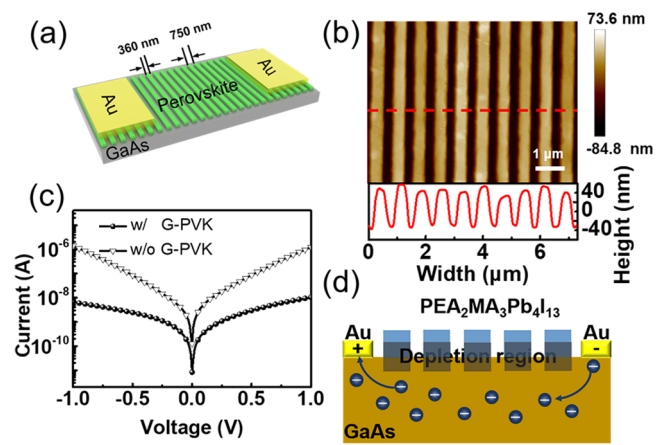


Fig. 1. (a) Schematic of GaAs photodetector with G-PVK. (b) AFM image (top panel) and the height profile (bottom panel) of the G-PVK. (c) $I - V$ curves of GaAs photodetectors with and without G-PVK-PD in the dark. (d) Working mechanism of GaAs photodetector with G-PVK in the dark.

meter (Thorlabs GmbH., PM 100D) before measurement. The transient photoresponse was characterized in a lab-built system, in which a signal generator (Tektronix, TDS2022B) was employed to connect the laser diode to produce pulsed light of varied frequencies, and an oscilloscope (Tektronix, TDS2012B) was used to record the electrical signal. For the polarization-sensitive detection, a polarizer was placed between the light source and the detector. A polarized light with different polarization angle with respect to the longitudinal orientation of the G-PVK was generated by continually rotating the polarizer.

III. RESULTS AND DISCUSSION

The schematic of GaAs photodetector with G-PVK is presented in Fig. 1(a). AFM image [Fig. 1(b)] reveals that the gratings display a uniform structure, with the typical width, height, and period of about 360, 85, and 750 nm, respectively. Current–voltage ($I - V$) curves of the devices in the dark are measured and plotted in Fig. 1(c). Notably, the dark current of the device with G-PVK is about two orders of magnitude lower than that of the control device. This could be understood by the working mechanism of the device shown in Fig. 1(d). When n-type GaAs is in contact with p-type G-PVK, electrons would diffuse from GaAs to PVK and holes would diffuse from PVK to GaAs until their Fermi levels are aligned at the same energy level. What is more, the electron carrier concentration of GaAs [23] is much higher than that of PVK [24], [25], which facilitates the effective diffusion of electrons from GaAs to PVK. A built-in electric field (a depletion region) with the direction from GaAs to PVK would then be produced at the interface. Therefore, the majority (electrons) in the superficial GaAs underneath G-PVK would be depleted, resulting in a high-resistance channel on the surface and leading to a lower dark current in the device.

Fig. 2(a) plots the $I - V$ curves of the GaAs photodetector with G-PVK upon illumination with different wavelengths. Clearly, the photodetector shows prominent photoresponse to incident light with broadband wavelengths (365–970 nm),

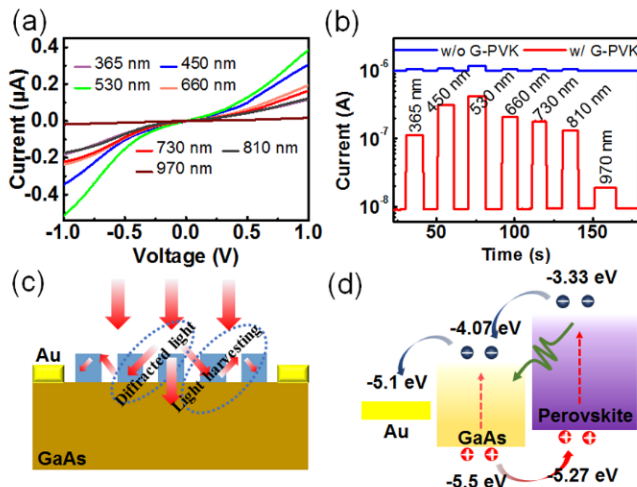


Fig. 2. (a) $I - V$ curves of the GaAs photodetector with G-PVK upon illumination with varied wavelengths (light intensity: 2.5 mW/cm^2) at 1-V bias. (b) Time-dependent photoresponse of the device with and without G-PVK. (c) Schematic of the diffraction in the structure. (d) Energy band diagram of the device under light illumination.

giving a peak photoresponse at 530 nm. This is well consistent with the reported absorption edge of $\text{PEA}_2\text{MA}_3\text{Pb}_4\text{I}_{13}$ [26], suggesting the high absorption of the G-PVK in the device. Nonlinear curves reveal the existence of Schottky barrier between GaAs and the metal electrodes. Although the current upon illumination is still lower than that of the control device, the ON/OFF ratio $I_{\text{light}}/I_{\text{dark}}$ (I_{light} and I_{dark} denote the current upon illumination and in the dark, respectively) increases from about 1.2 to 45 [Fig. 2(b)]. What is more, the photocurrent ($I_{\text{ph}} = I_{\text{light}} - I_{\text{dark}}$) of GaAs with G-PVK was higher than that of the control device over the broad wavelength range. For 530-nm illumination, the enhancement reached about 115%. This is reasonable since, for the incident visible light, the first-order diffraction exists in the diffraction grating with a period of 750 nm [27]. As shown in Fig. 2(c), when diffraction occurred, diffraction light could be reflected and diffracted multiple times within the structure, leading to an enhanced light trapping and light harvesting efficiency. On the other hand, the vertical built-in electric field between GaAs and PVK also contributes to the enhanced photocurrent. As illustrated in the band diagram shown in Fig. 2(d), when the device was illuminated by incident light with photon energy higher than the bandgap of PVK (1.93 eV), the photogenerated carriers were generated in both GaAs and PVK layer. Those within or near the depletion region could be spatially separated by the built-in electric field. The holes would be swept into PVK and trapped there, while the electrons would be swept into the GaAs channel. The recombination of photogenerated electrons and holes would be greatly suppressed due to the spatial separation, leading to a higher photocurrent [28], [29]. When the photon energy was higher than the bandgap of GaAs (1.43 eV) but lower than that of PVK, absorption occurred mostly in the GaAs layer. The photocurrent decreased slightly. However, the vertical built-in electric field still worked, giving rise to an enhanced photocurrent than the control GaAs photodetector.

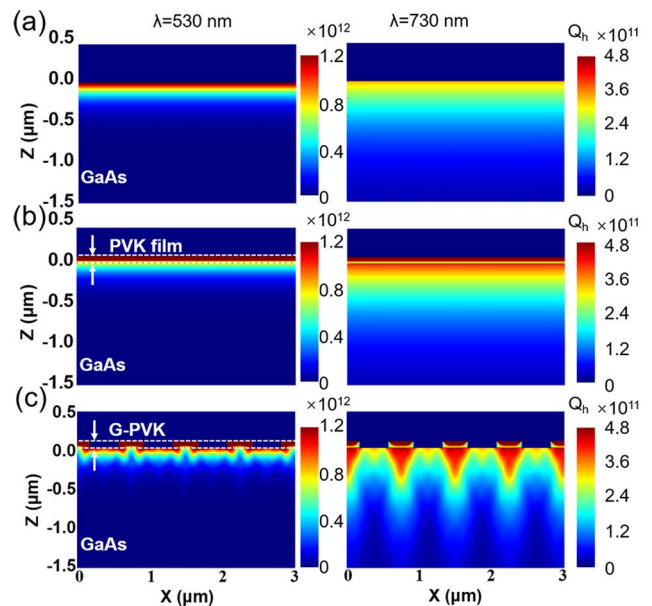


Fig. 3. FEM simulations of photon energy loss in (a) GaAs, (b) GaAs with PVK film, and (c) GaAs with G-PVK upon 530- and 730-nm illumination, respectively.

To gain physical insight into the effect of G-PVK on the enhanced photoresponse, a finite-element method (FEM) was employed to simulate absorption of the incident light in GaAs with and without G-PVK. The structure parameters of the device were obtained from the AFM image shown in Fig. 1(b). The incident light was set as a plane wave along the z -axis and the spatial mesh grids were set as physical field control grid. Periodic boundary conditions on both sides were added to simulate an infinite number of grating cells. Fig. 3 presents the simulated loss of photon energy (Q_h) in GaAs, GaAs with PVK thin film, and GaAs with G-PVK upon 530-nm (left) and 730-nm (right) illumination. It could be clearly observed that enhanced energy loss exists at the diffraction grating center of the device with G-PVK [Fig. 3(c)]. The energy loss under the diffraction grating increased with increasing the wavelengths. This could be ascribed to the synergetic effect of absorption and diffraction. Stronger absorption under 530-nm incident light led to weaker diffraction, while for 730-nm incident light (the photon energy higher than the bandgap of GaAs but lower than that of PVK), the absorption in the PVK layer was pretty low. The diffraction was greatly enhanced, giving rise to an enhanced absorption in the GaAs layer at the diffraction grating center. Therefore, a broadband enhancement of absorption was achieved.

The photoresponse of the GaAs photodetector with G-PVK depends strongly on the incident light intensity. Fig. 4(a) presents the $I - V$ curves of the device upon 530-nm illumination with varied light intensities. The current increased gradually from 12 to 1063 nA with the incident light intensity (P) increased from $4.98 \mu\text{W/cm}^2$ to 8.9 mW/cm^2 . This could be ascribed to the increased photogenerated carriers at a higher intensity. Photocurrent as a function of light density was fitted by the power law $I_{\text{ph}} \propto P^\theta$, showing the exponent θ of

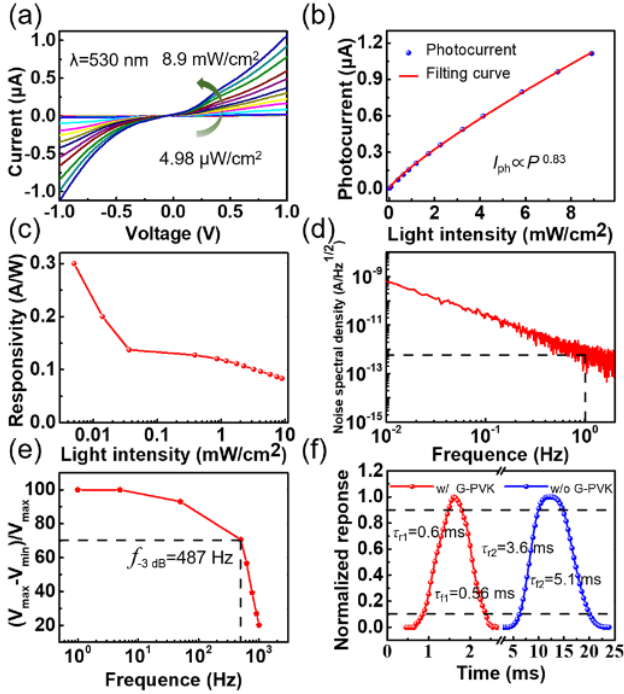


Fig. 4. (a) I - V curves of GaAs photodetector with G-PVK upon 530-nm illumination with varied light intensities. (b) Photocurrent as a function of light intensity at 1-V bias. (c) Responsivity as a function of the light intensity. (d) Noise spectral density based on the fast Fourier transform of the dark current. (e) Relative balance $(V_{\max} - V_{\min})/V_{\max}$ versus switching frequency of incident light. (f) Single magnified photoresponse for determining the rise/fall time.

0.83 [Fig. 4(b)]. This suggests a lower recombination loss in the device [30]. Furthermore, responsivity (R) and specific detectivity (D^*) of the device were calculated according to the equations [31], [32]

$$R = I_{\text{ph}}/(P \cdot S) \quad (1)$$

$$\text{NEP} = \overline{i_n^2}^{1/2}/R \quad (2)$$

$$D^* = (S\Delta f)^{1/2}/\text{NEP} \quad (3)$$

where S , NEP , $\overline{i_n^2}^{1/2}$, and Δf denote the effective illumination area of the device, noise equivalent power, the root-mean-square value of noise current, and the bandwidth, respectively. As plotted in Fig. 4(c), R decreased with the increase of light intensity and reached 0.3 A/W at a low light intensity of $4.98 \mu\text{W}/\text{cm}^2$, which is comparable to that of the commercial GaAs photodetector [33]. The noise spectral density at 1-Hz bandwidth was deduced to be $5.2 \times 10^{-13} \text{ A}/\text{Hz}^{1/2}$ from the fast Fourier transform (FFT) of the dark current [Fig. 4(d)]. Therefore, the highest D^* was calculated to be 2.24×10^{10} Jones, which is much larger than that of the control device without G-PVK (1.19×10^9 Jones). The -3 -dB bandwidth of the device (the frequency at which the photoresponse dropped to 70.7% of the highest value) was estimated to be around 487 Hz from the frequency-dependent relative balance $(V_{\max} - V_{\min})/V_{\max}$ shown in Fig. 4(e), which enables the device to monitor the optical signal over a wide switching frequency range. The rise time and fall time at a switching frequency of 500 Hz were estimated to be approximately

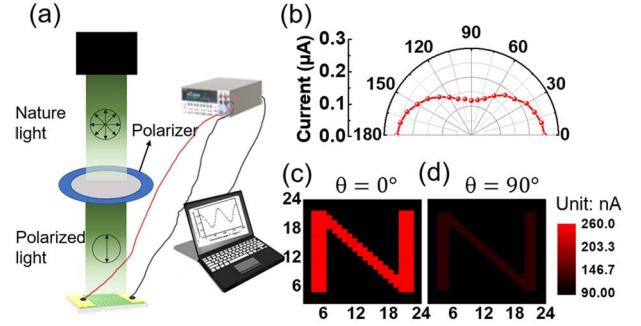


Fig. 5. (a) Schematic demonstration of polarization-sensitive photodetection. (b) Dependence of photocurrent on the polarization angle (0° - 180°). The 2-D current contrast map upon polarized illumination with the polarization angle of (c) 0° and (d) 90° .

0.6 and 0.56 ms from a single amplification period [red in Fig. 4(f)], which is faster than that of the control device [blue in Fig. 4(f)] and even comparable to the response time (0.5/0.35 ms for rise/fall time, respectively) of graphene/GaAs heterojunction photodetector [34].

It is also found that our photodetector with G-PVK was sensitive to polarized light [Fig. 5(a)]. As we could observe from Fig. 5(b), the photocurrent presents a strong dependence on the polarization angle. The maximum and minimum photocurrents emerged with the polarization angle of $0^\circ/180^\circ$ (the polarization direction parallel to the gratings) and 90° (the polarization direction perpendicular to the gratings), giving the peak-to-valley ratio I_{\max}/I_{\min} of 2.14, which was comparable to that of well-crystallized inorganic perovskite nanowires such as CsPbBr_3 nanowires (2.6) [35] and β - CsPbI_3 nanowires (2.68) [36]. The high polarization sensitivity of the device also endows its application in the field of polarization imaging [37]. For the single-pixel imaging, a hollow “N” pattern was laid between the polarizer and the device attached to a platform. The platform was driven by a stepper motor to move progressively along the x - and y -axes with a step length of 1.5 mm. The polarized light penetrating the hollow pattern was projected onto the device, and the photocurrent of each pixel was recorded and then integrated into a 24×24 two-dimensional contrast map. Clearly, the shape of the “N” pattern could be clearly identified with a suitable spatial resolution for the polarized light with a polarization angle of 0° [Fig. 5(c)]. When the polarization angle increased to 90° , the pattern can hardly be identified. This suggests that GaAs photodetector with well-aligned G-PVK had a potential application for polarization-sensitive imaging.

IV. CONCLUSION

In summary, GaAs photodetector with G-PVK has been fabricated through imprinting by a PDMS template obtained from a commercially available DVD-R master template. Due to the effective spatial separation of carriers by the vertical built-in electric field between GaAs and G-PVK, the dark current of the device was suppressed by two orders of magnitude when compared to the control GaAs photodetector. The photoresponse over the broad range was enhanced up to 215%

by the trapping effect arising from the diffraction grating, showing a responsivity of 0.3 A/W, a specific detectivity of 2.24×10^{10} Jones, and 0.6/0.56 ms for rise/fall time under 530-nm illumination, respectively. The device also presents a high sensitivity to the polarized light with a peak-to-valley ratio I_{\max}/I_{\min} of about 2.14, revealing the potential application of GaAs photodetector with well-aligned G-PVK in the polarization-sensitive imaging system.

REFERENCES

- [1] A. Mukherjee, D. Ren, P. E. Vullum, J. Huh, B. O. Fimland, and H. Weman, "GaAs/AlGaAs nanowire array solar cell grown on Si with ultrahigh power-per-weight ratio," *ACS Photon.*, vol. 8, no. 8, pp. 2355–2366, Aug. 2021, doi: [10.1021/acsphotonics.1c00527](https://doi.org/10.1021/acsphotonics.1c00527).
- [2] Z. Xu *et al.*, "Monolayer MoS₂/GaAs heterostructure self-driven photodetector with extremely high detectivity," *Nano Energy*, vol. 23, pp. 89–96, May 2016, doi: [10.1016/j.nanoen.2016.03.011](https://doi.org/10.1016/j.nanoen.2016.03.011).
- [3] C. Jia *et al.*, "A self-powered high-performance photodetector based on a MoS₂/GaAs heterojunction with high polarization sensitivity," *J. Mater. Chem. C*, vol. 7, no. 13, pp. 3817–3821, Mar. 2019, doi: [10.1039/c8tc06398b](https://doi.org/10.1039/c8tc06398b).
- [4] H. Dejun, L. Guohui, Y. Feng, and E. J. Zhu, "Ultrahigh-sensitive AlGaAs-GaAs punchthrough heterojunction phototransistor," *IEEE Photon. Technol. Lett.*, vol. 9, no. 10, pp. 1391–1393, Oct. 1997, doi: [10.1109/jtph.1997.623273](https://doi.org/10.1109/jtph.1997.623273).
- [5] N. Matsuo, H. Ohno, and H. Hasegawa, "Mechanism of high gain in GaAs photoconductive detectors under low excitation," *Jpn. J. Appl. Phys.*, vol. 23, no. 5A, pp. L299–L301, May 1984, doi: [10.1143/jjap.23.L299](https://doi.org/10.1143/jjap.23.L299).
- [6] H. Beneking, "Gain and bandwidth of fast near-infrared photodetectors: A comparison of diodes, phototransistors, and photoconductive devices," *IEEE Trans. Electron Devices*, vol. ED-29, no. 9, pp. 1420–1431, Sep. 1982, doi: [10.1109/t-ed.1982.20892](https://doi.org/10.1109/t-ed.1982.20892).
- [7] Q. Lyu, H. Jiang, and K. M. Lau, "High gain and high ultraviolet/visible rejection ratio photodetectors using p-GaN/AlGaIn/GaN heterostructures grown on Si," *Appl. Phys. Lett.*, vol. 117, no. 7, Aug. 2020, Art. no. 071101, doi: [10.1063/5.0011685](https://doi.org/10.1063/5.0011685).
- [8] C. Y. Wu *et al.*, "Controlled synthesis of GaSe microbelts for high-gain photodetectors induced by the electron trapping effect," *J. Mater. Chem. C*, vol. 8, no. 16, pp. 5375–5379, Apr. 2020, doi: [10.1039/d0tc01120g](https://doi.org/10.1039/d0tc01120g).
- [9] H. C. Lee and B. V. Zeghbroeck, "A novel high-speed silicon MSM photodetector operating at 830 nm wavelength," *IEEE Electron Device Lett.*, vol. 16, no. 5, pp. 175–177, May 1995, doi: [10.1109/55.382231](https://doi.org/10.1109/55.382231).
- [10] M. Mikulics *et al.*, "Ultrafast and highly sensitive photodetectors with recessed electrodes fabricated on low-temperature-grown GaAs," *IEEE Photon. Technol. Lett.*, vol. 18, no. 7, pp. 820–822, Apr. 1, 2006, doi: [10.1109/lpt.2006.871696](https://doi.org/10.1109/lpt.2006.871696).
- [11] O. M. Maragò, P. H. Jones, P. G. Gucciardi, G. Volpe, and A. C. Ferrari, "Optical trapping and manipulation of nanostructures," *Nature Nanotechnol.*, vol. 8, no. 11, pp. 807–819, Nov. 2013, doi: [10.1038/nnano.2013.208](https://doi.org/10.1038/nnano.2013.208).
- [12] W. Wang and L. Qi, "Light management with patterned micro and nanostructure arrays for photocatalysis, photovoltaics, and optoelectronic and optical devices," *Adv. Funct. Mater.*, vol. 29, no. 25, Apr. 2019, Art. no. 1807275, doi: [10.1002/adfm.201807275](https://doi.org/10.1002/adfm.201807275).
- [13] M. L. Brongersma, Y. Cui, and S. Fan, "Light management for photovoltaics using high-index nanostructures," *Nature Mater.*, vol. 13, pp. 451–460, Apr. 2014, doi: [10.1038/nmat3921](https://doi.org/10.1038/nmat3921).
- [14] Y. C. Lee, C. C. Chang, and Y. Y. Chou, "Experimental and simulation studies of anti-reflection sub-micron conical structures on a GaAs substrate," *Opt. Exp.*, vol. 21, no. S1, pp. A36–A41, Jan. 2013, doi: [10.1364/oe.21.000a36](https://doi.org/10.1364/oe.21.000a36).
- [15] H. Wang *et al.*, "Nanoimprinted perovskite nanograting photodetector with improved efficiency," *ACS Nano*, vol. 10, no. 12, pp. 10921–10928, Dec. 2016, doi: [10.1021/acs.nano.6b05535](https://doi.org/10.1021/acs.nano.6b05535).
- [16] Y. Wang, M. Li, X. Zhou, P. Li, X. Hu, and Y. Song, "High efficient perovskite whispering-gallery solar cells," *Nano Energy*, vol. 51, pp. 556–562, Sep. 2018, doi: [10.1016/j.nanoen.2018.06.085](https://doi.org/10.1016/j.nanoen.2018.06.085).
- [17] W. Tian, L. Min, F. Cao, and L. Li, "Nested inverse opal perovskite toward superior flexible and self-powered photodetection performance," *Adv. Mater.*, vol. 32, no. 16, Apr. 2020, Art. no. 1906974, doi: [10.1002/adma.201906974](https://doi.org/10.1002/adma.201906974).
- [18] Y. Zhan *et al.*, "A butterfly-inspired hierarchical light-trapping structure towards a high-performance polarization-sensitive perovskite photodetector," *Angew. Chem.*, vol. 131, no. 46, pp. 16608–16614, Nov. 2019, doi: [10.1002/anie.201908743](https://doi.org/10.1002/anie.201908743).
- [19] F. Li *et al.*, "Ambipolar solution-processed hybrid perovskite phototransistors," *Nature Commun.*, vol. 6, no. 1, Sep. 2015, Art. no. 8238, doi: [10.1038/ncomms9238](https://doi.org/10.1038/ncomms9238).
- [20] S. Shrestha *et al.*, "High-performance direct conversion X-ray detectors based on sintered hybrid lead triiodide perovskite wafers," *Nature Photon.*, vol. 11, no. 7, pp. 436–440, Jun. 2017, doi: [10.1038/nphoton.2017.94](https://doi.org/10.1038/nphoton.2017.94).
- [21] R. Huang, D. H. Lin, J. Y. Liu, C. Y. Wu, D. Wu, and L. B. Luo, "Nanochannel-confined growth of crystallographically orientated perovskite nanowire arrays for polarization-sensitive photodetector application," *Sci. China Mater.*, vol. 64, no. 10, pp. 2497–2506, Oct. 2021, doi: [10.1007/s40843-021-1654-5](https://doi.org/10.1007/s40843-021-1654-5).
- [22] Y. Xie, H. Yu, J. Duan, L. Xu, and B. Hu, "Enhancing device performance in quasi-2D perovskite ((BA)₂(MA)₃Pb₄I₁₃) solar cells using PbCl₂ additives," *ACS Appl. Mater. Interface*, vol. 12, no. 9, pp. 11190–11196, Mar. 2020, doi: [10.1021/acsami.9b21163](https://doi.org/10.1021/acsami.9b21163).
- [23] S. Sze and J. Irvin, "Resistivity, mobility and impurity levels in GaAs, Ge, and Si at 300°K," *Solid-State Electron.*, vol. 11, no. 6, pp. 599–602, Jun. 1968, doi: [10.1016/0038-1101\(68\)90012-9](https://doi.org/10.1016/0038-1101(68)90012-9).
- [24] P. N. Rudd and J. Huang, "Metal ions in halide perovskite materials and devices," *Trends Chem.*, vol. 1, no. 4, pp. 394–409, Jul. 2019, doi: [10.1016/j.trechm.2019.04.010](https://doi.org/10.1016/j.trechm.2019.04.010).
- [25] W. Peng *et al.*, "Ultralow self-doping in two-dimensional hybrid perovskite single crystals," *Nano Lett.*, vol. 17, no. 8, pp. 4759–4767, Aug. 2017, doi: [10.1021/acs.nanolett.7b01475](https://doi.org/10.1021/acs.nanolett.7b01475).
- [26] Y. Yan *et al.*, "Air-stable and self-driven perovskite photodiodes with high on/off ratio and swift photoresponse," *Small*, vol. 14, no. 41, Oct. 2018, Art. no. 1802764, doi: [10.1002/sml.201802764](https://doi.org/10.1002/sml.201802764).
- [27] Y. Wang *et al.*, "Diffraction-grated perovskite induced highly efficient solar cells through nanophotonic light trapping," *Adv. Energy Mater.*, vol. 8, no. 12, Apr. 2018, Art. no. 1702960, doi: [10.1002/aenm.201702960](https://doi.org/10.1002/aenm.201702960).
- [28] L. Luo *et al.*, "A highly sensitive perovskite/organic semiconductor heterojunction phototransistor and its device optimization utilizing the selective electron trapping effect," *Adv. Opt. Mater.*, vol. 7, no. 13, May 2019, Art. no. 1900272, doi: [10.1002/adom.201900272](https://doi.org/10.1002/adom.201900272).
- [29] Q. Zhao *et al.*, "The role of traps in the photocurrent generation mechanism in thin InSe photodetectors," *Mater. Horizons*, vol. 7, no. 1, pp. 252–262, Jan. 2020, doi: [10.1039/c9mh01020c](https://doi.org/10.1039/c9mh01020c).
- [30] F. P. G. de Arquer, A. Armin, P. Meredith, and E. H. Sargent, "Solution-processed semiconductors for next-generation photodetectors," *Nature Rev. Mater.*, vol. 2, no. 3, pp. 1–17, Mar. 2017, doi: [10.1038/natrevmats.2016.100](https://doi.org/10.1038/natrevmats.2016.100).
- [31] J. W. Lim *et al.*, "Self-powered reduced-dimensionality perovskite photodiodes with controlled crystalline phase and improved stability," *Nano Energy*, vol. 57, pp. 761–770, Mar. 2019, doi: [10.1016/j.nanoen.2018.12.068](https://doi.org/10.1016/j.nanoen.2018.12.068).
- [32] C. Xie, P. You, Z. Liu, L. Li, and F. Yan, "Ultrasensitive broadband phototransistors based on perovskite/organic-semiconductor vertical heterojunctions," *Light. Sci. Appl.*, vol. 6, no. 8, p. e17023, Aug. 2017, doi: [10.1038/lsa.2017.23](https://doi.org/10.1038/lsa.2017.23).
- [33] X. Chen *et al.*, "Analysis of the influence and mechanism of sulfur passivation on the dark current of a single GaAs nanowire photodetector," *Nanotechnology*, vol. 29, no. 9, Mar. 2018, Art. no. 095201, doi: [10.1088/1361-6528/aaa4d6](https://doi.org/10.1088/1361-6528/aaa4d6).
- [34] Z. Tao *et al.*, "Graphene/GaAs heterojunction for highly sensitive, self-powered visible/NIR photodetectors," *Mater. Sci. Semicond. Process.*, vol. 111, Jun. 2020, Art. no. 104989, doi: [10.1016/j.mssp.2020.104989](https://doi.org/10.1016/j.mssp.2020.104989).
- [35] J. Feng *et al.*, "Crystallographically aligned perovskite structures for high-performance polarization-sensitive photodetectors," *Adv. Mater.*, vol. 29, no. 16, Apr. 2017, Art. no. 1605993, doi: [10.1002/adma.201605993](https://doi.org/10.1002/adma.201605993).
- [36] Y. Zhou *et al.*, "Flexible linearly polarized photodetectors based on all-inorganic perovskite CsPbI₃ nanowires," *Adv. Opt. Mater.*, vol. 6, no. 22, Nov. 2018, Art. no. 1800679, doi: [10.1002/adom.201800679](https://doi.org/10.1002/adom.201800679).
- [37] Q. Song *et al.*, "Moiré perovskite photodetector toward high-sensitive digital polarization imaging," *Adv. Energy Mater.*, vol. 11, no. 29, Aug. 2021, Art. no. 2100742, doi: [10.1002/aenm.202100742](https://doi.org/10.1002/aenm.202100742).